A Model for the Behavior of Battery Separators in Compression at Different Strain/Charge Rates

Gennady Y. Gor,[a,*,z] **John Cannarella,**[b,*] **Jean H. Prévost,**[a] **and Craig B. Arnold**[b,**]

[a]*Department of Civil and Environmental Engineering, Princeton University, Princeton, New Jersey 08544, USA*
[b]*Department of Mechanical and Aerospace Engineering, Princeton University, Princeton, New Jersey 08544, USA*

During charge and discharge of a lithium battery, intercalation of lithium ions into the electrodes can cause their noticeable expansion, compressing the soft separator between them. To assess the role of these effects on the battery performance, it is necessary to know the response of the battery separator under compressive loading. Here we develop a model for predicting the elastic response of a commercial separator immersed in fluid to compression at different strain rates. We show that the response of the separator is determined by combination of viscoelastic behavior of the polymer skeleton and poroelastic behavior, due to the flow of the fluid in the pores. Poroelastic behavior causes effective stiffening of the separator, which increases with the strain rate. For a sample of ca. 1 cm in diameter these effects become pronounced at strain rates $\gtrsim 10^{-3}$ s^{-1} and have to be taken into account in coupled mechano-electrochemical models for lithium-ion batteries.

During the operation of a lithium ion battery, in addition to electrochemical processes, mechanical evolution of the battery's components also takes place. When a battery is charging or discharging, lithium ions intercalate into the electrodes. The intercalation causes measurable expansion of the typical electrode materials used in commercial cells: lithium cobalt oxide expands by as much as 2%, while graphite electrode particles have been shown to expand by up to 10%.[1] For novel high capacity anode materials the expansion can be even higher, for instance, silicon can reach as high as 400% expansion.[2] The expanding electrodes, constrained by the cell assembly, compress the thin porous separator leading to pore shrinkage and even closure,[3,4] so that the ion transport decreases and the battery performance deteriorates.[5] In order to understand the consequences of compressive loads on the separator for battery performance, a coupled mechano-electrochemical model for the lithium-ion cell is necessary. Development of such a model requires the knowledge of mechanical properties of the separator.

Review papers focusing on the separator properties limit the summary of the mechanical properties to the data obtained from the tensile testing of dry materials.[6,7] More recently Halalay et al.[8] used the nanoindentation method to determine the elastic modulus and the hardness of different separators. Chen et al.[9] carried on ex situ tensile testing of the separator under an atomic force microscope to determine mechanisms of its fracturing and failure. These papers also considered the properties of the dry materials, while, in a battery, the separator is always fully immersed in a fluid: a solution of the electrolyte salt in the organic solvent.

The effects of long-time immersion on the mechanical performance and durability of the polypropylene (PP) separators were studied recently by Love.[10] He showed that properties of the separator before and after 4-weeks immersion in the electrolyte solution differ insignificantly. Sheidaei et al.[11] performed the tensile tests of Celgard 2400 polypropylene separator during immersion in the electrolyte solution and a pure carbonate solvent. They used 1.1 M LiPF$_6$ solution in the mixture of ethylene carbonate (EC) and dimethyl carbonate (DMC), and pure DMC for their tests and found that the mechanical properties of dry materials noticeably differ from the properties of the immersed separator: the effective Young's modulus of the wet separator is almost two times lower than that of the dry. These studies were

further extended by Avdeev et al.;[12] they observed that the same softening effect of DMC takes place for three-layer (PP-PE-PP) Celgard C480 separator. They also reported noticeable change of mechanical properties of both dry and wet separator with the strain rate and temperature: the separator is effectively stiffer at higher strain rates or lower temperatures.

Although the tensile tests of a fluid-immersed separator provide more insights on the separator behavior in the battery than the dry tests, they still do not represent the realistic loading conditions. In the battery the loads on a separator are compressive, both due to electrode swelling upon lithium intercalation and stacking loads.[13] Since the separators have complex anisotropic structure, and mechanical properties in lateral ("machine") direction and transverse direction are noticeably different,[11] it is not viable to predict the behavior in compression based on the properties obtained from tensile tests.

In our previous work we present the results of compressive tests of commercial macroporous semi-crystalline polypropylene (PP) separator Celgard 3501 at different strain rates in dry and wet conditions.[14] The microstructure of this separator is shown on the SEM on the Figure 1. The experiments were carried out with three different fluids: water, DMC and electrolyte solution (1 M LiPF$_6$ solution in 1:1 EC/DMC mixture). We focused on two characteristic mechanical properties of the separator: effective Young's modulus determined in the region of small deformation, and flow stress. We found that both of these properties differ for the dry material and immersed in fluid. We also found strong dependence of both on the strain rate; this dependence qualitatively differs from that for the values determined in the tensile tests.[11,12] Particularly, we observed the noticeable stiffening of the wet sample at high strain rates. This effect cannot be explained by viscoelastic properties of the polymer, and should be attributed to poroelastic behavior.

By poroelastic behavior we mean the response of a porous material saturated with fluid subjected to compression, which differs from a response of a non-porous solid. The compressive stress, in addition to the deformation of the body, squeezes the fluid from the pores. The viscous flow of the fluid induces additional resistance to the compression, making the body effectively stiffer. This phenomenon is crucial for geotechnical engineering, to predict the response of water-saturated soils to the loads. Theory of poroelasticity (or poromechanics) has been developed in the works of Terzaghi[15] and Biot,[16] and in more advanced formulation by Rice and Cleary.[17] The detailed state of the art formulation can be found in.[18]

*Electrochemical Society Student Member.
**Electrochemical Society Active Member.
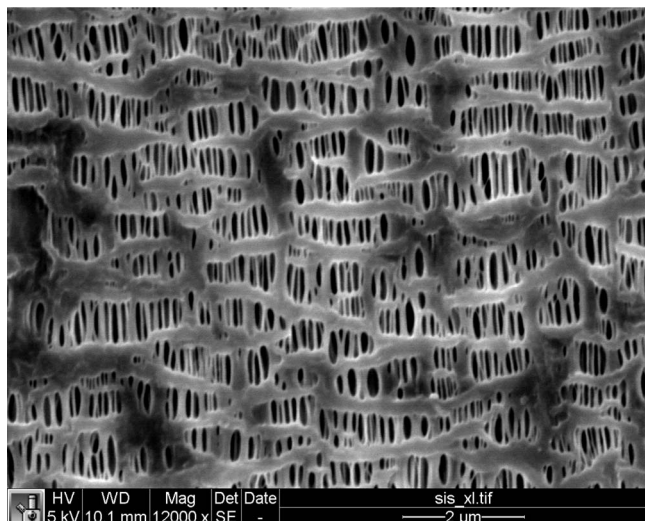zE-mail: ggor@princeton.edu

Figure 1. SEM image of the Celgard 3501 separator used in experiments in the plane perpendicular to the compression.

In the current work we develop a quantitative model for the compressive behavior of the separator based on viscoelasticity and poroelasticity. Our model is capable for determination of the materials parameters relevant to the compression of the separator during battery operation. We performed simulations using Dynaflow finite element code[19] and calculated the effective Young's modulus corresponding to the experimental conditions. First we performed the calculations within the linear elastic model for the solid matrix, which gave qualitative agreement with the experiments. Then we took into account the non-linear viscoelastic behavior of the PP from the effective modulus of the dry material as a function of the strain rate. Viscoelastic behavior of the polymer skeleton and poroelastic behavior of the immersed separator provide quantitative agreement between the simulated results and experimental data. Our model shows that for a sample of ca. 1 cm in diameter immersed in LiPF$_6$ solution in the poroelastic effects become pronounced at strain rates $\gtrsim 10^{-3}$ s^{-1}, and have to be taken into account in coupled mechano-electrochemical models for lithium-ion batteries.

Behavior of Dry Separator

Since the thickness of the separator is only 25 μm, it is not feasible to perform the compression tests with a single sheet. Therefore, several layers stacked together were used in this testing. The sample is circular with the diameter 3/8 inches (ca. 1 cm). Figure 2 shows a schematic of the experimental setup used in.[14]
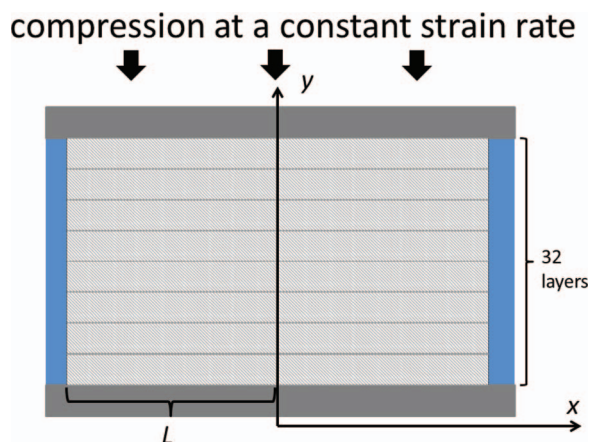

Figure 2. Schematic of the experimental setup for compressive testing of the separator. Direction of compression is perpendicular to the plane shown in Figure 1.
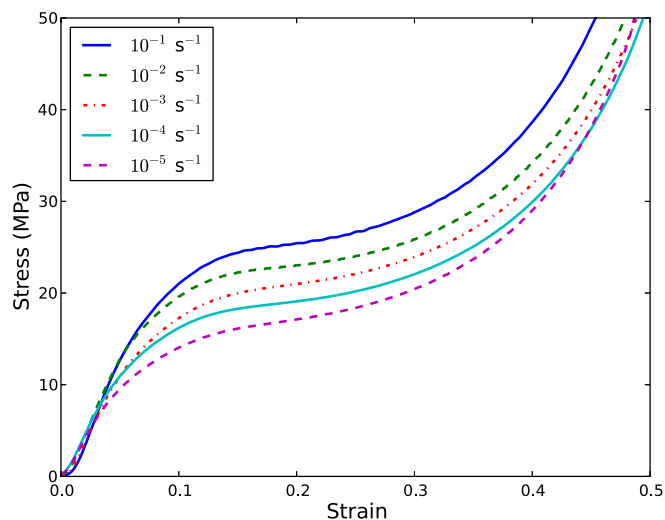

Figure 3. Stress-strain curves for the compression of the dry separator at constant strain rates.

The compressive tests were performed over a wide range of strain rates using a commercial Instron machine (model 5969). The results from these experimental tests given in [14] demonstrate that the separator mechanical properties exhibit noticeable strain rate dependence. Figure 3 presents the stress-strain curves for the compression of the dry separator at the constant strain rates from 10^{-5}–10^{-1} s^{-1}, showing the increase of the effective Young's modulus and the flow stress.

Even at the small strains, the slope of the stress-strain curve changes, therefore, in [14] we determine the effective Young's modulus as the maximum slope of the curve (which corresponds roughly to 2-3% deformation). The flow stress is determined as the stress corresponding to strain 20% at which the elasticity of the separator (slope of the stress-strain curve) noticeably decreases.[14] Figure 4 gives the effective Young's modulus E_{eff} and flow stress σ^{flow} as functions of the strain rate. It is clearly seen that both values increase linearly as a function of logarithm of the strain rate $\dot{\epsilon}$ and can be fit with the following simple two-parameter formulas

$$E = E_0 + C_E \log\left(\dot{\epsilon}/10^{-5}\right), \qquad [1]$$

$$\sigma^{\text{flow}} = \sigma_0^{\text{flow}} + C_\sigma \log\left(\dot{\epsilon}/10^{-5}\right). \qquad [2]$$

Here the strain rate $\dot{\epsilon}$ is in s^{-1}, the parameters E_0 and σ_0^{flow} correspond to the slow strain rate $\dot{\epsilon} = 10^{-5}$ s^{-1} and C_E and C_σ are constants, log is the common logarithm. Fitting the experimental data shown in Figure 4 gives $E_0 = 247$ MPa, $C_E = 23.2$ MPa and $\sigma_0^{\text{flow}} = 17.6$ MPa and $C_\sigma = 1.99$ MPa.

Strain-rate dependent effects for the dry sample can be attributed to viscoelastic properties of the PP. Xiao and co-workers used linear viscoelastic model to fit the experimental tensile data.[11,20] Linear viscoelastic models are based on the representation of the polymer as a combination of Hookean springs and Newtonian dashpots (mathematically presented in the form of Prony series) and fit the stress-strain curve at a given constant strain rate.[11] While the linear viscoelastic model works well at a given strain rate, it fails when attempted to use for different strain rates. In particular, the linear model cannot explain the logarithmic increase of the effective Young's modulus and flow stress.

It is worth noting that the logarithmic relations between the mechanical properties of the polymer and the strain rate are in line with the Eyring's theory.[21,22] Within the Eyring's theory deformation of polymers is considered as a thermally activated rate process in which the segments of the polymer chains cross potential barriers. Applied stress change the potential barriers, so that (unlike the linear model) the viscosity of the polymer becomes stress-dependent, and the flow
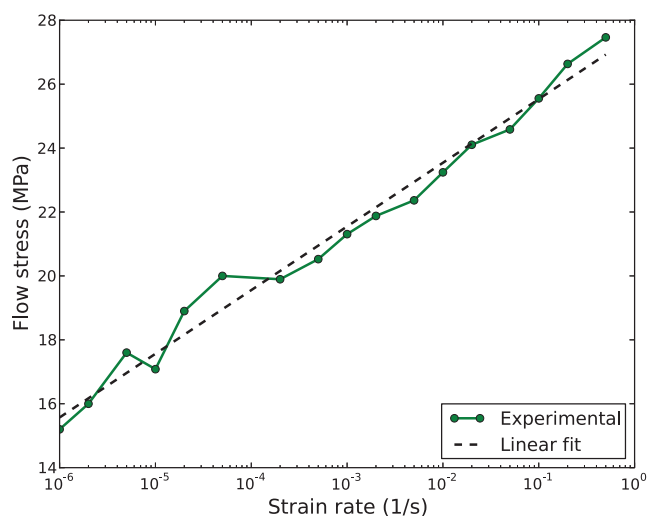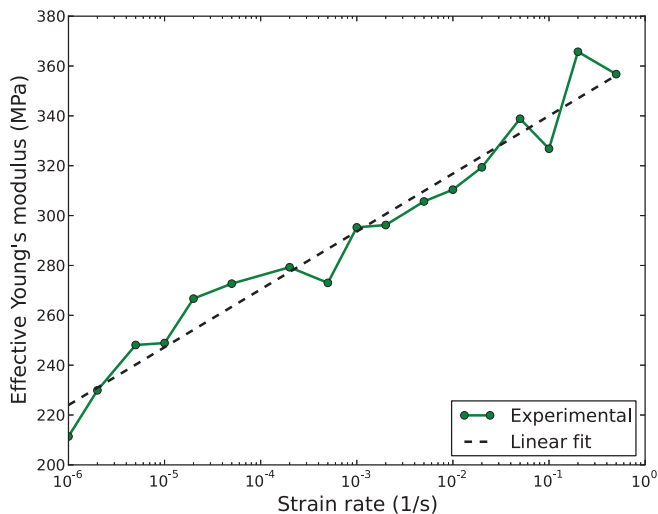
Figure 4. Effective Young's modulus (top) and flow stress (bottom) of the dry separator as a function of the strain rate.

Figure 5. Experimental stress-strain curves for the separator immersed in water.

in our case consists of microscopic PP fibers and plates) and fluid, which fills all the pore space. The amount of voids (or pores) is determined by the porosity of the system, which is the ratio of the volume of the pores V_p to the total volume of the body V, $\phi \equiv V_p/V$. The fluid flow in the porous body is described in terms of permeability k, which depends on the characteristic pore sizes, structure and connectivity.

The stress-strain relation has to take into account deformation of the pore space, non-porous polymeric skeleton and the fluid flow. Therefore, Hooke's law does not hold even in the case of small strains and has to be augmented with the term related to the fluid pressure p. A general relation for the linear poroelastic solid is:[18]

$$\epsilon_{ij} = \frac{1+\nu}{E}\left(\sigma_{ij} + bp\delta_{ij}\right) - \frac{3\nu}{E}\left(\sigma + bp\right)\delta_{ij}. \qquad [4]$$

Here ϵ_{ij} is the strain tensor, σ_{ij} is the total stress tensor, $\sigma = \sigma_{kk}/3$, δ_{ij} is the Kronecker delta, ν, E are the bulk properties of dry ("drained") porous matrix (Poisson's ratio and Young's modulus), and b is the Biot's coefficient, which is the key property of the porous matrix. This relation takes into account that the deformation of the porous solid is caused by the so-called effective stress, which includes the

of the polymer (the strain rate) is related to the applied stress by nonlinear function. In the case of high stresses or high strain rates it gives the exponential function, qualitatively explaining the relations 1 and 2:[23]

$$\dot{\epsilon} \simeq A\exp(B\sigma). \qquad [3]$$

Behavior of Immersed Separator

The experimental results reported in our previous publication[14] revealed that the response of the separator immersed in fluid in the compression tests noticeably differs from the response of the dry separator. Figure 5 presents the experimental stress-strain curves for the separator immersed in water. Figure 6 shows the effective Young's modulus derived from these curves and from the stress-strain curves for the separator immersed in DMC and in LiPF6 solution, shown along with the effective modulus of the dry separator for comparison. Although both dry and wet separator becomes effectively stiffer at higher strain rates, the stiffening of the wet separator is more pronounced and simple logarithmic relation Eq. 1 does not hold anymore. In our previous publication[14] we assigned this effect to the poroelastic response and here we add the quantitative analysis to this phenomenon.

Governing equations for poroelastic behavior.— We consider a porous solid body consisting of two continua: a porous matrix, (which
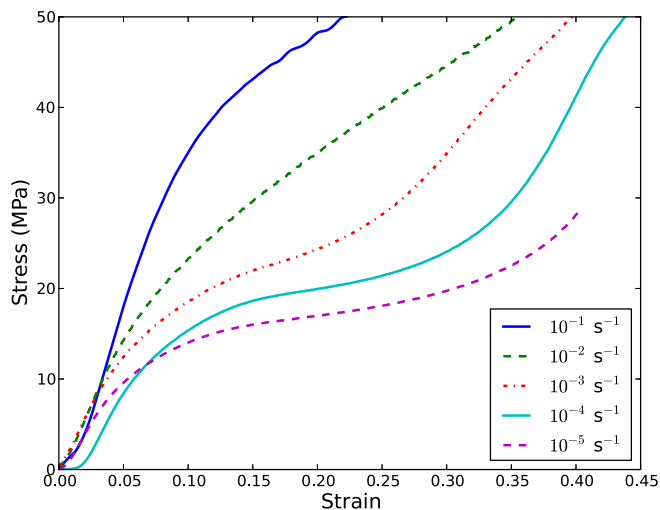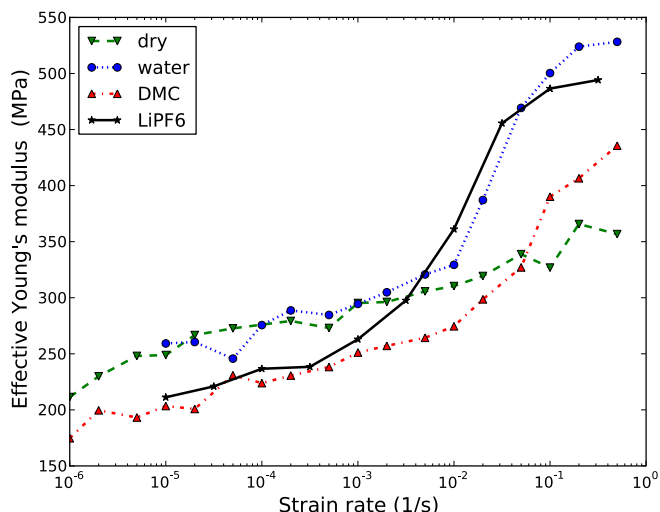

Figure 6. Effective Young's modulus of the dry separator, immersed in water, in DMC and in 1 M LiPF$_6$ solution in EC/DMC.

contribution from the fluid pressure in the pores

$$\sigma'_{ij} = \sigma_{ij} + bp\delta_{ij}. \qquad [5]$$

The Biot's coefficient b quantifies the part of the volumetric strain caused by the change of porosity and is defined as

$$b = 1 - \frac{K}{K_s}, \qquad [6]$$

where K and K_s are the bulk moduli of the porous matrix and non-porous "skeleton particles" respectively (grains in the case of soil, or bulk PP in our case). Biot coefficient ranges between 0 and 1 with $b \to 0$ corresponding to deformation of non-porous solid and $b \to 1$ corresponding to deformation of the porous material with incompressible skeleton particles, where all the strain is due to the change of void space.

The pressure value $p = p(\mathbf{r}, t)$ in Eq. 4 is governed by the following equation[16]

$$\frac{1}{M}\frac{\partial p}{\partial t} + b\frac{\partial \epsilon}{\partial t} = \frac{k}{\mu}\nabla^2 p, \qquad [7]$$

where ϵ is the volumetric strain, μ is the fluid viscosity and the modulus M is determined by

$$\frac{1}{M} = \left[\frac{\phi}{K_f} + \frac{b-\phi}{K_s}\right], \qquad [8]$$

K_f is the bulk modulus of the fluid.

Introducing the Cartesian coordinates x and y, shown on the Figure 2 and z perpendicular to the plane of that Figure, the stress-strain equation 4 can be written as

$$\epsilon_x = \frac{1}{E}\left[\sigma_x - \nu(\sigma_y + \sigma_z)\right] + (1-2\nu)\frac{bp}{E}, \qquad [9]$$

and similarly to other components. To interpret the results of our experiments it is sufficient to consider the problem in two dimensions, i.e. we do not consider the z direction, and consider rectangular domain similarly to the classical Mandel problem.[24] The measurement of the total thickness of the stack of the separators suggests that there are no gaps between the separator and the plates (and between the separator sheets). Therefore, we assume that the fluid cannot leak from the top and bottom of the separator stack. Also, based on the information about the separator microstructure,[25] we assume that the flow (the pressure evolution) takes place only along one horizontal axis, e. g. the x axis. Therefore, $p(\mathbf{r}, t) = p(x, t)$ and the so boundary conditions for the pressure equation are the following:

$$p(x,t)|_{t=0} = 0 \quad p(x,t)|_{x=L} = 0 \quad \left.\frac{\partial p(x,t)}{\partial x}\right|_{x=0} = 0, \qquad [10]$$

where L is the radius of the sample (or half of the length for the 2D representation).

Since the separator is not constrained in the x direction, $\sigma_x = 0$, and the stress-strain relation Eq. 9 for the vertical stress becomes

$$\sigma_y(x,t) = E\epsilon_y(t) - (1-2\nu)bp(x,t) \qquad [11]$$

Finally, to get the stress-strain relation for the sample as a whole and derive the effective modulus E_{eff} we need to solve the pressure equation 7 and average Eq. 11 along the top surface of the sample

$$\langle\sigma_y\rangle = \frac{1}{L}\int_0^L \sigma_y(x',t)dx' = E\epsilon(t) - \frac{(1-2\nu)b}{L}\int_0^L p(x',t)dx'. \qquad [12]$$

The effective Young's modulus, determined in experiments can be obtained from Eq. 12

$$E_{\text{eff}} \equiv \frac{\langle\sigma_y\rangle}{\epsilon(t)} = E - \frac{(1-2\nu)b}{L\epsilon(t)}\int_0^L p(x',t)dx'. \qquad [13]$$

Note that in compression $\epsilon(t) \leq 0$, and therefore the second term in Eq. 13 is positive, so $E_{\text{eff}} \geq E$, i.e. the sample is effectively stiffer.

Table I. Material Properties used in simulations

Fluid Properties	
Bulk modulus K_f (water)	2 GPa
Bulk modulus K_f (DMC)	1 GPa
Bulk modulus K_f (LiPF$_6$ solution)	1 GPa
Viscosity μ (water)	1 mPa · s
Viscosity μ (DMC)	0.6 mPa · s
Viscosity μ (LiPF$_6$ solution)	4.2 mPa · s
Skeleton Particles Properties	
Bulk modulus K_s (PP)	4 GPa
Porous Matrix Properties	
Porosity φ	0.515
Young's modulus E	247 MPa
Poisson's ratio ν	0.0
Bulk modulus K	82 MPa
Biot coefficient b	0.98
Permeability k	10^{-16} m^2

Material parameters.— Description of behavior of a porous body filled with a fluid requires use of material parameters, related to fluid, solid skeleton particles and porous matrix. The parameters used in our model are summarized in Table I. The DMC properties are readily available in literature.[26,27] The viscosity of the electrolyte solution (1 M LiPF$_6$ solution in EC/DMC) is given in [28]; the bulk modulus of this solution is not known, so the value for DMC is used. For the bulk modulus of the non-porous constituent we took a typical value for PP.[29] The porosity of the matrix is determined from the density measurement, the Young's modulus is determined from our compression tests at low strain rates ($\dot\epsilon = 10^{-5}$ s^{-1}).[14] The compression experiments did not show any noticeable change of the separator cross section;[14] therefore we assume the Poisson's ratio of the porous matrix equal to exactly zero. To assess the effect of the matrix Poisson's ratio, we performed calculations for using different values of this parameter. In these calculations, for each value of the ν we calculated the bulk modulus of the matrix K and then used Eq. 6 to calculate the Biot's coefficient.

The permeability of the separator is another parameter which is difficult to determine experimentally. However, an order-of-magnitude estimate can be made based on the experimental data for effective Young's modulus. The pressure equation 7 is a diffusion type equation with the coefficient[17,18]

$$c_f = \frac{k}{\mu}C, \qquad [14]$$

where

$$C \equiv \frac{M(1-\nu)}{1-\nu + b^2(1-2\nu)(1+\nu)M/E}. \qquad [15]$$

Therefore the characteristic "diffusion" time is given by

$$\tau_D \sim L^2/c_f. \qquad [16]$$

Poroelastic effects become noticeable when the time of deformation at which we consider the effective system properties $\tau_\epsilon \sim \epsilon/\dot\epsilon$ ($\epsilon \simeq 2\%$ in our case) is of the same order as the diffusion time: $\tau_\epsilon \sim \tau_D$. Figure 6 shows that the effective modulus of the sample immersed in water starts to deviate from the modulus of the dry sample at the strain rate $\sim 10^{-2}$ s^{-1}. Assuming that this strain rate corresponds to $\tau_\epsilon \sim \tau_D$, according to Eq. 14, we have

$$k \sim \frac{\mu L^2 \dot\epsilon}{C\epsilon}. \qquad [17]$$

Eq. 17 for the parameters of our problem gives $k \sim 10^{-16}$ m^2. We used this value in our simulations, but in addition to that, in order to assess the effect of the permeability on the effective modulus, we also performed calculations for $k \sim 10^{-15}$ m^2 and $k \sim 10^{-17}$ m^2.
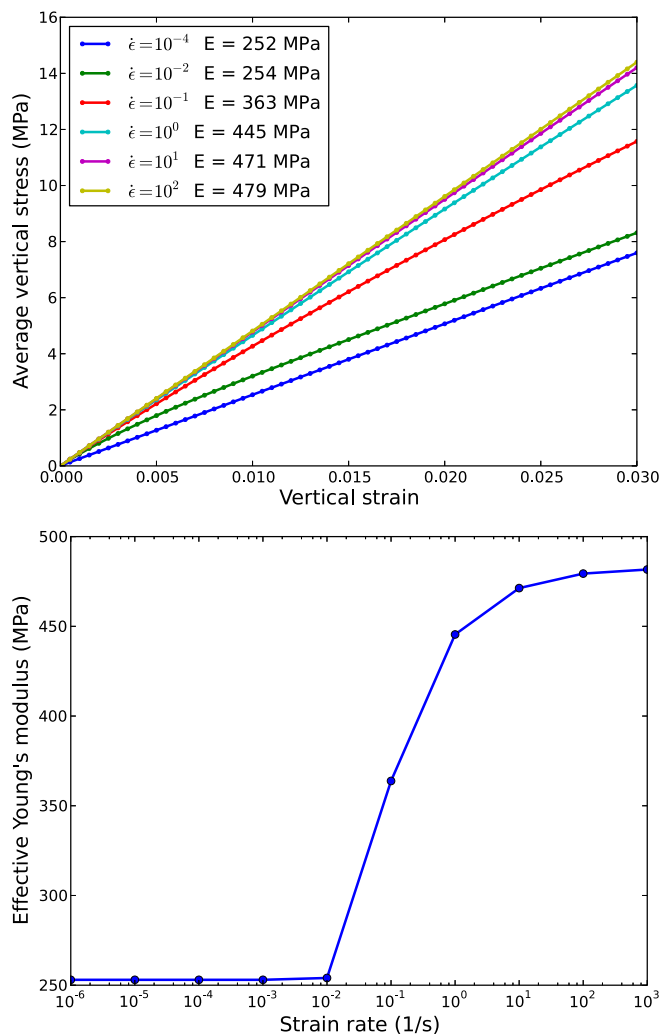
Figure 7. (top) Stress-strain curves calculated from finite-element simulations of vertical compression of porous separator at selected strain rates (bottom) Effective Young's modulus estimated from these stress-strain curves as a slope at 2% strain.

Figure 8. Effective Young's modulus calculated based on poroelasticity (top) for $v = 0$ and different values of permeability k (bottom) for $k = 10^{-16}$ m^2 and different values of Poisson's ratio v.

Simulation results.— We solve the equations 7 and 11 with the boundary conditions 10 using the Dynaflow finite-element code.[19] In our simulations we consider a half of the 2D domain shown in Figure 2. We use 2D rectangular mesh 200 × 10 elements ($x \times y$). Selected simulations were also checked on a finer mesh to ascertain the absence of meshing effects. For all the tests the calculated reactions at the top elements were then integrated according to Eq. 12 to get the resulting stress-strain curves. In order to stay within the limits of linear poroelasticity, all of the simulations were performed for the maximum strain 3%.

The top panel of Figure 7 shows the stress-strain curves predicted from the finite element simulations of compression of the separator at different strain rates. Higher strain rates result in a steeper stress-strain curves, and therefore higher effective Young's moduli. The effective moduli calculated from the slopes of the stress-strain curves are shown in the bottom panel of the figure. As seen from the stress-strain curves in Figure 7, the slope is changing. We calculated the effective modulus as the slope at 2% strain in order to be consistent with the data reported in.[14]

At low strain rates ($\leq 10^{-4}$ s^{-1} and below) the response of the separator corresponds to the "fully drained" response: the compression is so slow that the fluid has enough time to escape from the pores ($\tau_\epsilon \gg \tau_D$). At high strain rates ($\geq 10^2$ s^{-1} and above), the response is "fully undrained": the compression is so fast that the fluid does not
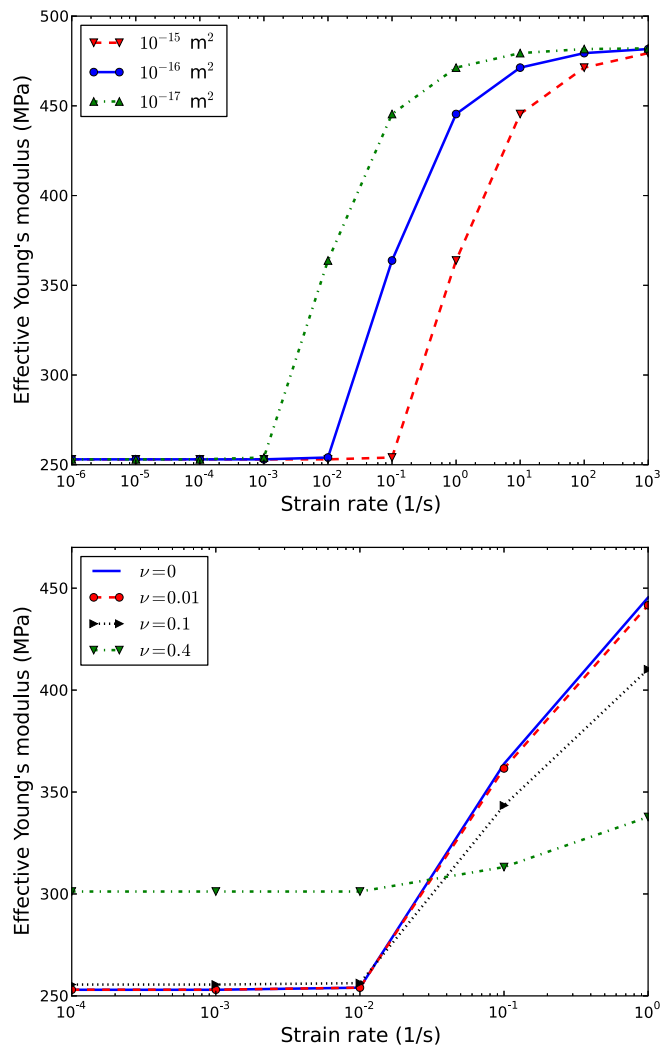
have time to flow from the pores ($\tau_\epsilon \ll \tau_D$). In this case the effective Young's modulus is noticeably higher because it involves compression of the fluid trapped in the pores.

Since two of the materials parameters (permeability of the separator k and the Poisson's ratio v) are hard to determine precisely, we performed a parametric study on them. Figure 8 shows the effective Young's modulus of the separator immersed in water as a function of strain rate. Top panel shows that the change of permeability does not affect the shape of the curve, nor the difference between the drained and undrained response. Higher permeability will just shift the curve to the right, so that fully undrained response will take place at higher strain rates. This plot gives an additional guidance for choosing the value of the permeability for our system.

The bottom panel gives the effective Young's modulus of the separator as a function of the strain rate calculated for different values of Poisson's ratio. Poisson's ratio affects the Biot's coefficient and thus it is responsible for the difference between the minimum value of the modulus (fully drained response) and maximum value (fully undrained response). These calculations show that for small Poisson's ratios (0.0, 0.01, 0.1) the predictions are close and justify the use of $v = 0.0$ in the calculations for the sake of simplicity.

Comparison to experimental data.— We use the materials parameters summarized in Table I and simulate the compression of the
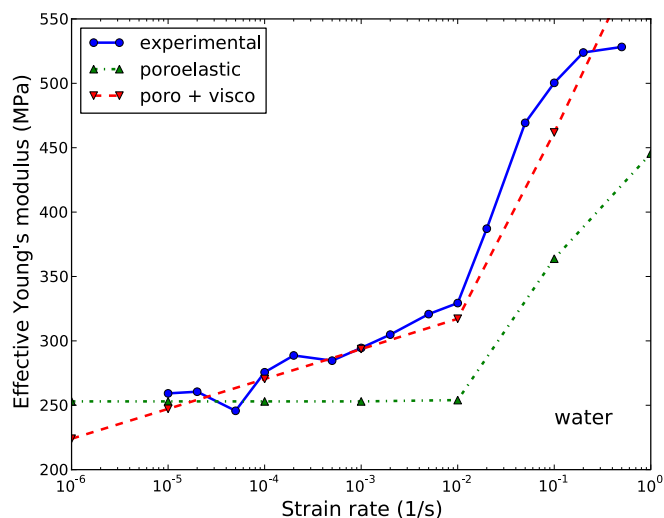
Figure 9. Effective Young's modulus of the separator immersed in water as a function of strain rate. The solid line gives the experimental data from [14], the dash-dot line shows the calculations based on linear poroelastic behavior of the dry separator; and the dash line shows the calculations taking into account viscoelastic behavior of the dry separator when solving the equations of poroelasticity.
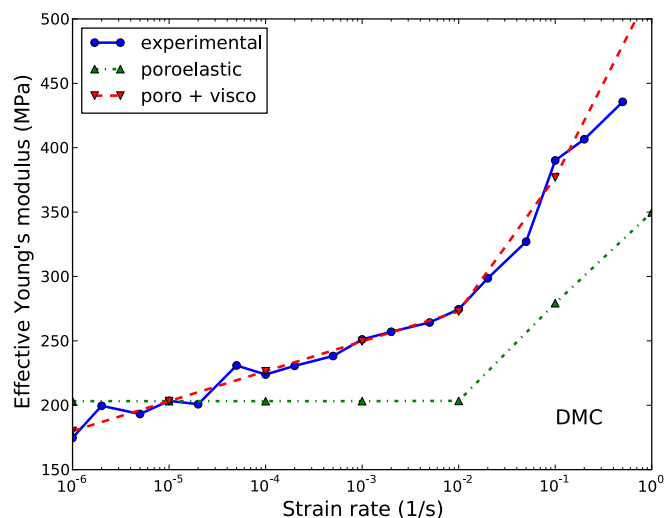

Figure 10. Effective Young's modulus of the separator immersed in DMC as a function of strain rate. Solid line represents the experimental data from [14], dash-dot line shows the results of calculations based on linear poroelastic behavior of the dry separator; red line shows the results of calculations, which take into account viscoelsatic behavior of the dry separator and softening of the separator in DMC when solving the equations of poroelasticity.

separator immersed in water at the constant strain rates corresponding to the rates used in our experiments.[14] For each of the strain rates we calculate the effective Young's modulus based on the algorithm described above. Figure 9 shows the experimental values of the effective Young's modulus of the immersed separator[14] (solid line) and two series of calculations. The first series (shown in dash-dot line) is based on linear poroelastic behavior of the dry separator. Although this series gives the same trend as the experimental curve, it noticeably underestimates the increase of the effective modulus. The second series (dash line) takes into account the increase of the modulus of dry porous matrix E with the increase of the strain rate representing the viscoelastic properties of the PP. This dependence was implemented by using in the simulations the strain-rate dependent Young's modulus of the matrix given by Eq. 1. Figure 9 shows that the latter series agrees well to the experimentally observed modulus. We have to note, that to take into account viscoelasticity one cannot simply substitute Eq. 1 into Eq. 13. Modification of the Young's modulus of the porous matrix change the value of Biot's coefficient, which affects the second term in Eq. 13.

Then we calculate the effective Young's modulus of the separator immersed in DMC and LiPF$_6$ solution. Figures 10 and 11 show experimental data from [14], and two series of calculations for each of the fluids. Similarly to Figure 9, one series is based on poroelastic model, and another takes into account the viscoelasticity. Unlike the case of water (shown in Figure 9), when separator is immersed in DMC or LiPF$_6$ solution additional softening is observed at small strain rates. In our simulations we took into account this softening by systematically reducing the Young's modulus of the porous matrix by 44 MPa and 36 MPa correspondingly. These values are obtained by comparison of the moduli of dry material and immersed in DMC and LiPF$_6$ solution at the strain rate 10^{-5} s^{-1}.

The matrix Poisson's ratio ν and permeability k were determined based on the comparison with water-immersed data, and used here as input parameters. Since these values provide reasonable agreement for the experimental data on the samples immersed in DMC and LiPF$_6$ solution, it confirms our estimates.

Discussion

Our previous work[14] showed that the mechanical properties of battery separator in compression tests noticeably differ from the prop-

erties, derived in tensile test. Moreover, the effects of fluid on the elastic response differ in tension and in compression. Compression tests, which unlike the tensile tests, represent loads relevant to the loads on the separator in a battery, showed very pronounced stiffening of the separator at high strain rates. Here we developed a simple model, which explains this response as a combination of viscoelastic behavior of the separator matrix and poroelastic behavior – flow of the fluid in the pore space. The predictions based on our model are close to the experimental data, and the small deviations observed can be attributed to the rough estimates for permeability and Poisson's ratio of the porous matrix used for calculations.

The estimates from [14] show that for a conventional graphite anode the charge rate of 1 C corresponds to the compression of the
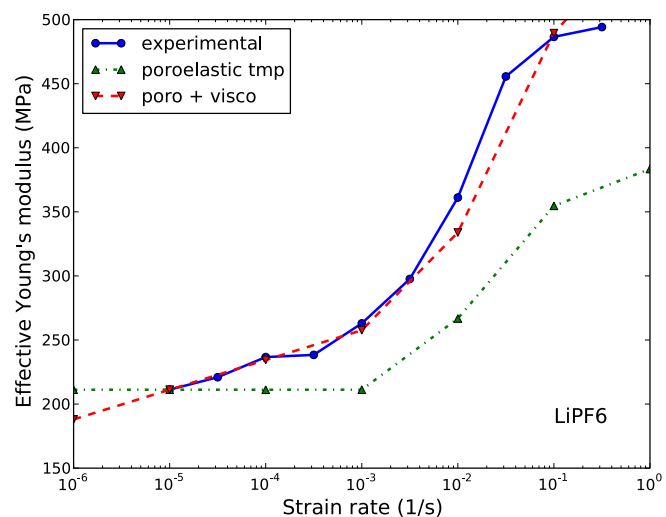

Figure 11. Effective Young's modulus of the separator immersed in 1 M LiPF$_6$ solution in EC/DMC as a function of strain rate. Solid line represents the experimental data from,[14] dash-dot line shows the results of calculations based on linear poroelastic behavior of the dry separator; red line shows the results of calculations, which take into account viscoelsatic behavior of the dry separator and softening of the separator in solution when solving the equations of poroelasticity.

separator at the strain rate 10^{-4} s^{-1}. Therefore, for the small separators considered in this work, the poroelastic effects need to be taken into account only at relatively high charge rates, ca. 10 C and above. However, several factors affect this estimate. If considering novel anode material with higher expansion upon intercalation (e.g. silicon), same charge rate can cause noticeably higher strain rate. Poroelastic effects may also become pronounced at lower strain rates in case if the permeability of the separator is lower, or the viscosity of the fluid is higher. LiPF$_6$ solution, which is more viscous than water and DMC, starts to show the poroelastic effects at lower strain rates than the latter two. Also the diffusion time, which determines the poroelastic effects, strongly depends on the length of the separator: it is proportional to the square of the sample length (Eq. 16). Therefore for large format lithium-ion batteries, where the characteristic size of the separator is of order of 10 cm,[30] the poroelastic effects can be highly pronounced at charge rates below 1 C.

Higher strain rates are also typically used when the tensile/compression tests are performed in the laboratory to derive the materials parameters; as such Avdeev et al. used $10^{-1} - 10^{-3}$ s^{-1} for the tensile measurements.[12] In the case of compression tests, the results at these strain rates would be strongly affected by the poroelastic effects, and have to be taken into account when estimating the material parameters. Based on our model, the materials parameters can be obtained from the fast experiments and extrapolated to predict behavior of materials at slow strain rates. It saves time for testing required to estimate the materials parameters.

Our model relies on the assumption of linear poroelasticity based on the small strains. Therefore, we did not consider high strains and yielding of the separator here. However, experiments show that dependence of the flow stress on the strain rate is the same as the Young's modulus.[14] Therefore, the model for predicting the effective Young's modulus also provide information about the flow stress. Particularly, we can conclude that the experimentally observed values of the flow stress[14] are also determined by combination of viscoelasticity and poroelasticity.

Although the current work is focused specifically on behavior of the separators in lithium-ion batteries, our results can be useful for other applications. Particularly, the model which combines linear poroelasticity and non-linear viscoelasticity can be employed for predicting mechanical behavior of macroporous polymers immersed in fluids used as proton exchange membranes in fuel cells.

While our model takes into account the mechanical effects of the fluid on the effective elasticity of the separator, it cannot predict which fluids cause the softening of the separator (e.g. DMC or LiPF$_6$ solution) and which do not (e.g. water). These effects are determined by the specifics of interactions between the molecules of the fluid and of the separator, they cannot be explained within a purely mechanistic model and require discussion of the chemical properties of fluid-separator systems beyond the scope of the current paper. Another path for further extension of our model could be account for the temperature effects, since the mechanical properties of the PP separators are shown to be sensitive to it.[10,12]

Conclusions

During charge and discharge of a battery, the electrodes expand and contract due to intercalation of lithium ions. Expanding electrodes compress the soft separator between them, affecting the transport of ions through it. To assess the role of these effects on the battery performance, it is necessary to know the response of the battery separator under compressive loading. Here we develop a model for predicting the elastic response of a commercial porous polypropylene separator immersed in fluid to compression at different strain rates, representing a range of charge rates. We show that the complex behavior of the separator is determined by combination of viscoelastic behavior of the polymer skeleton and poroelastic behavior, related to the flow of the fluid in the pores. Poroelastic behavior causes pronounced effective stiffening of the separator, which increases with the strain rate. For the small separator size (ca. 1 cm diameter) considered in this work, the poroelastic effects are manifested at strain rates above 10^{-3} s^{-1}, which correspond to the charge rates 10 C and above. However, poroelastic effects are determined by the pressure diffusion time, which is proportional to the square of the the sample size (Eq. 16). Therefore, for large format lithium-ion cells where the separator size is ca. 10 cm, the poroelastic effects will be pronounced at strain rates which are two orders of magnitude lower and correspond to charge rates 0.1 C. Viscoelastic behavior takes place within the whole range of strain rates studied, and it gives a simple logarithmic dependence for the effective modulus.

The results of our work will be further used in the development of predictive model for studying the coupled mechanics and electrochemistry of lithium-ion batteries. Such model can serve as a tool for optimization the materials and geometric parameters of lithium-ion cells to find a path toward extending their performance and lifecycle.

References

1. Y. Qi, H. Guo, L. G. Hector, and A. Timmons, *J. Electrochem. Soc.*, **157**, A558 (2010).
2. U. Kasavajjula, C. Wang, and A. J. Appleby, *J. Power Sources*, **163**, 1003 (2007).
3. C. Peabody and C. B. Arnold, *J. Power Sources*, **196**, 8147 (2011).
4. Y. Pan and Z. Zhong, *J. Electrochem. Soc.*, **161**, A583 (2014).
5. J. Cannarella and C. B. Arnold, *J. Power Sources*, **226**, 149 (2013).
6. P. Arora and Z. J. Zhang, *Chem. Rev.*, **104**, 4419 (2004).
7. S. S. Zhang, *J. Power Sources*, **164**, 351 (2007).
8. I. C. Halalay, M. J. Lukitsch, M. P. Balogh, and C. A. Wong, *J. Power Sources*, **238**, 469 (2013).
9. J. Chen, Y. Yan, T. Sun, Y. Qi, and X. Li, *RSC Advances*, **4**, 14904 (2014).
10. C. T. Love, *J. Power Sources*, **196**, 2905 (2011).
11. A. Sheidaei, X. Xiao, X. Huang, and J. Hitt, *J. Power Sources*, **196**, 8728 (2011).
12. I. Avdeev, M. Martinsen, and A. Francis, *J. Mater. Eng. Perform.*, **23**, 315 (2014).
13. J. Cannarella and C. B. Arnold, *J. Power Sources*, **245**, 745 (2014).
14. J. Cannarella, X. Y. Liu, C. Leng, P. Sinko, G. Y. Gor, and C. B. Arnold, *J. Electrochem. Soc.*, this issue (2014).
15. K. Terzaghi, *Theoretical Soil Mechanics* (John Wiley & Sons, New York, 1943).
16. M. A. Biot, *J. Appl. Phys.*, **12**, 155 (1941).
17. J. R. Rice and M. P. Cleary, *Rev. Geophys.*, **14**, 227 (1976).
18. O. Coussy, *Poromechanics* (John Wiley & Sons, 2004).
19. J. H. Prévost, *DYNAFLOW: A Nonlinear Transient Finite Element Analysis Program. Department of Civil and Environmental Engineering, Princeton University, Princeton, NJ. (last update 2014)* (1981), URL http://blogs.princeton.edu/prevost/dynaflow/.
20. W. Wu, X. Xiao, X. Huang, and S. Yan, *Comput. Mater. Sci.*, **83**, 127 (2014).
21. H. Eyring, *J. Chem. Phys.*, **4**, 283 (1936).
22. A. Tobolsky and H. Eyring, *J. Chem. Phys.*, **11**, 125 (1943).
23. I. M. Ward and J. Sweeney, *Mechanical Properties of Solid Polymers* (John Wiley & Sons, 2012).
24. J. Mandel, *Géotechnique*, **3**, 287 (1953).
25. M. Ebner and V. Wood, *personal communication* (2014).
26. A. Rodriguez, J. Canosa, A. Dominguez, and J. Tojo, *J. Chem. Eng. Data*, **48**, 146 (2003).
27. J. Zhou, R. Zhu, H. Xu, and Y. Tian, *J. Chem. Eng. Data*, **55**, 5569 (2010).
28. Y. R. Dougassa, J. Jacquemin, L. El Ouatani, C. Tessier, and M. Anouti, *J. Phys. Chem. B*, **118**, 3973 (2014).
29. R. Warfield and F. R. Barnet, Tech. Rep., DTIC Document (1972).
30. S. U. Kim, P. Albertus, D. Cook, C. W. Monroe, and J. Christensen, *J. Power Sources*, **268**, 625 (2014).